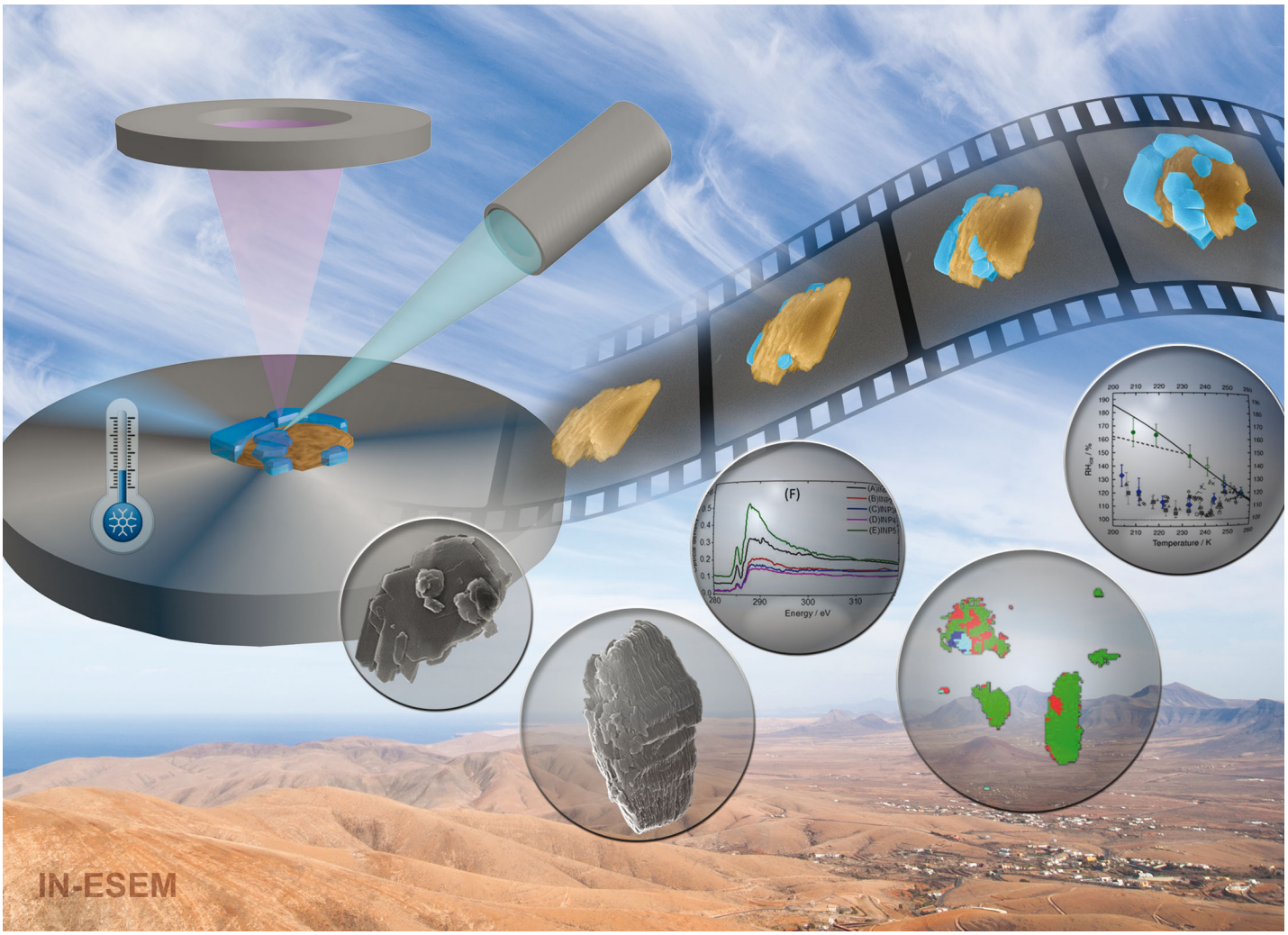

Showcasing the work at the Environmental Molecular Sciences Laboratory at Pacific Northwest National Laboratory.

Title: Direct observation of ice nucleation events on individual atmospheric particles

The work presents microscopic observations of heterogeneous ice nucleation from experiments conducted inside an environmental scanning electron microscope. Observations of ice formation on kaolinite particles demonstrate that ice preferentially nucleates at the edges of the stacked platelets, rather than on the basal planes. This platform is applied for directly detecting and tracking ice nucleating particles in ambient aerosol samples and is complemented by micro-spectroscopic chemical imaging. This technique opens a path to new physical chemistry studies of ice formation in atmospheric science, cryobiology, and material science.

As featured in:

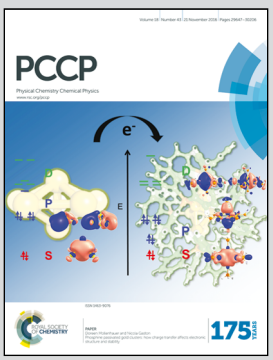

See Bingbing Wang *et al.*, *Phys. Chem. Chem. Phys.*, 2016, **18**, 29721.

ROYAL SOCIETY OF CHEMISTRY

www.rsc.org/pccp

Registered charity number: 207890

PCCP

PAPER

View Article Online
View Journal | View Issue

Cite this: *Phys. Chem. Chem. Phys.*, 2016, **18**, 29721

Direct observation of ice nucleation events on individual atmospheric particles†

Bingbing Wang,‡*[a] Daniel A. Knopf,[b] Swarup China,[a] Bruce W. Arey,[a] Tristan H. Harder,[cd] Mary K. Gilles[c] and Alexander Laskin[a]

Received 28th July 2016,
Accepted 14th September 2016

DOI: 10.1039/c6cp05253c

www.rsc.org/pccp

Heterogeneous ice nucleation is a physical chemistry process of critical relevance to a range of topics in the fundamental and applied sciences and technologies. Heterogeneous ice nucleation remains insufficiently understood, partially due to the lack of experimental methods capable of obtaining *in situ* microscopic details of ice formation over nucleating substrates or particles. We present microscopic observations of ice nucleation events on kaolinite particles at the nanoscale and demonstrate the capability of direct tracking and micro-spectroscopic characterization of individual ice nucleating particles (INPs) in an authentic atmospheric sample. This approach utilizes a custom-built ice nucleation cell, interfaced with an Environmental Scanning Electron Microscope (IN-ESEM platform) operated at temperatures and relative humidities relevant for heterogeneous ice nucleation. The IN-ESEM platform allows dynamic observations of individual ice formation events over particles in isobaric and isothermal experiments. Isothermal experiments on individual kaolinite particles demonstrate that ice crystals preferably nucleate at the edges of the stacked kaolinite platelets, rather than on their basal planes. These experimental observations of the location of ice nucleation provide direct information for further theoretical chemistry predictions of ice formation on kaolinite.

1. Introduction

The different phases of water (vapor, liquid water, and several forms of ice) are of interest to a broad range of scientific disciplines because of their fundamental importance to all aspects of life, environment, and technology. Ice can form through homogeneous and heterogeneous nucleation. If water or aqueous solutions are cooled down to the homogeneous freezing limit, then they can form ice spontaneously by homogeneous nucleation. However, ice can also form on a substrate by heterogeneous nucleation at higher temperatures that lie between the homogeneous freezing limit and the ice melting point. In the applied sciences, the heterogeneous nucleation of ice plays an important role in technologies of cryopreservation,[1–3] freeze-drying in biomedical research and the food industry,[4] and the development of anti-icing coatings for aircraft.[5,6] In atmospheric chemistry and physics, ice nucleation initiated by airborne particles governs the formation and microphysical properties of ice and mixed phase clouds.[7–10] However, the description of the physicochemical characteristics of particles which control the formation of atmospheric ice crystals is insufficient for the predictive understanding of their impacts on cloud formation, cloud life cycle, and thus, climate.

In the atmosphere, heterogeneous ice nucleation is initiated by airborne particles (ice nucleating particles, INPs), which frequently have complex multicomponent and multiphase composition. Heterogeneous ice nucleation can proceed *via* immersion freezing (ice forms on an INP suspended inside a supercooled droplet), deposition ice nucleation (ice nucleates from the supersaturated water vapor onto the solid INP surface), condensation freezing (ice forms after water vapor condenses onto an INP at supercooled conditions), and contact nucleation (ice forms in a supercooled droplet upon collision with an INP).[11] To advance our understanding of heterogeneous ice nucleation,

[a] *William. R. Wiley Environmental Molecular Sciences Laboratory, Pacific Northwest National Laboratory, Richland, WA 99352, USA*
[b] *Institute for Terrestrial and Planetary Atmospheres, School of Marine and Atmospheric Sciences, Stony Brook University, Stony Brook, NY 11794, USA*
[c] *Chemical Sciences Division, Lawrence Berkeley National Laboratory, Berkeley, California 94720, USA*
[d] *Department of Chemistry, University of California, Berkeley, California 94720, USA*

† Electronic supplementary information (ESI) available: Temperature calibration curve (Fig. S1); comparison of ice nucleation ability on kaolinite particles (Fig. S2); chemical characterization of atmospheric INPs by SEM/EDX (Fig. S3); ten isothermal ice nucleation experiments on kaolinite particles (Fig. S4 and S5); example of immersion freezing (Movie S1) and ice nucleating particle tracking (Movie S2); example of temperature and dew point calibration experiments (Movies S3 and S4); homogeneous condensation of water vapor on NaCl particles (Movie S5). See DOI: 10.1039/c6cp05253c

‡ Present address: State Key Laboratory of Marine Environmental Science (Xiamen University), College of Ocean and Earth Science, Xiamen University, Xiamen 361102, China. E-mail: Bingbing.Wang@xmu.edu.cn; Tel: +86-592-2880816.

an ideal laboratory experiment would allow *in situ* observation of the ice nucleation process on the nanoscale: something not possible in field studies.[7] Such an experiment would yield information on the composition and morphology of the individual INPs and the nucleation mechanisms.

Environmental scanning electron microscope (ESEM) allows direct, *in situ* observations of particle (or other substrate) hygroscopic transformations with tens of nanometer spatial resolution.[12–18] Hence, it represents a significant improvement over more commonly used optical microscopy (OM) approaches.[19–25] Complemented with X-rays microanalysis, ESEM has the potential to conduct microscopy studies of ice nucleation along with chemical characterization of the INPs. Currently, the limiting factor for ESEM ice nucleation experiments is the ability to accurately control temperature and relative humidity (RH) above the sample over a broad range of freezing temperatures. Understanding the propensity of INPs, relevant to the processes of atmospheric ice formation, requires experiments at precisely controlled cooling rates of less than 2 ± 0.2 K min^{-1}, down to temperatures of 190 K.[26–30] Recent ESEM experiments, using Peltier cooling stages, have examined the ice nucleation onsets of mineral dust INPs of known composition[31,32] and microscopic imaging of the ice surface topography[33] at temperatures as low as 233 K. However, experimental studies of atmospheric ice nucleation, and applications in cryo-biology[2,3,34] require experimental platforms that can probe wider ranges of low temperatures, cooling rates, and RH, and preferably, accompanied with physicochemical analysis of INPs or other samples.

In this work, we present ice nucleation studies using a novel ice nucleation-ESEM (IN-ESEM) experimental platform employing a custom-built cryogenic temperature controlled cell that allows experimental observation of ice nucleation over particles deposited on substrates. This platform allows precise control of temperature and RH with respect to ice (RH_{ice}), up to the water saturation conditions. Thus, it provides experimental coverage over the extreme conditions relevant for ice and mixed phase cloud formation in the atmosphere. We demonstrate capabilities of the IN-ESEM platform based on ice nucleation experiments over kaolinite particles. These experiments show that ice nucleates preferentially at the edges of the layered platelets of kaolinite. Theoretical chemistry simulations are necessary to improve our understanding of ice nucleation initiated by the edge sites of kaolinite.[35–37] An additional case investigation was also performed to demonstrate the capability of INP detection and tracking in a field-collected sample, complemented by chemical characterization of individual INPs.

2. Experimental section

2.1 Ice nucleation cell coupled to an environmental SEM (IN-ESEM)

Fig. 1 shows schematics of the ice nucleation cell and the experimental layout of the IN-ESEM platform. The ice nucleation cell is a custom-built, temperature-controlled cryo-stage based on a previously developed ice nucleation setup.[38,39] As shown in Fig. 1A, the main components of the ice nucleation cell include: a sample holder, a cryo-stage (cooling and heating elements), and a base attached to the SEM motorized stage. The sample is placed in the holder, which is then mounted, *via* an O-ring, to the cover of the cryo-cooling stage. The 0.2 mm^2 opening in the cover sealed with an O-ring resting on the sample allows exposure of the sample to water vapor present in the ESEM chamber. The temperature of the cryo-cooling stage is controlled by a resistively heated element (Minco Product Inc.) while constant cooling is provided by liquid nitrogen.

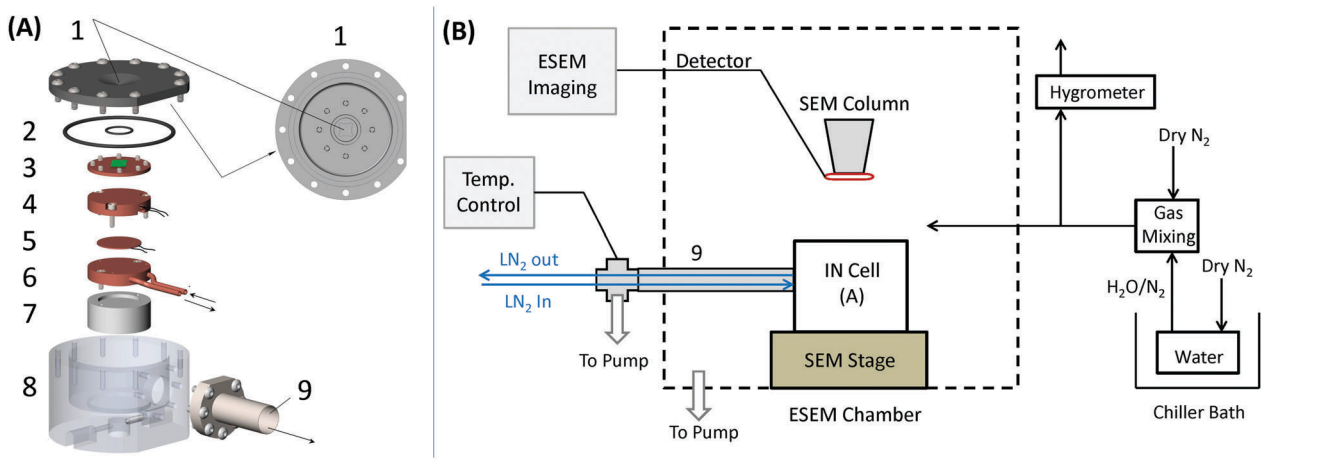

Fig. 1 Schematics of (A) the expanded view of the ice nucleation cell and (B) the experimental layout of the IN-ESEM system. Panel A: Ice nucleation cell components include: (1) cover with opening (0.5 mm in diameter) allowing sample exposure to water vapor and electron beam; (2) Viton O-rings for sealing; (3) sample holder (copper plate, brown) with a sample substrate (green square); (4) compartment for Pt-100 temperature sensor; (5) heating element; (6) liquid nitrogen (LN_2) cooling block; (7) spacer to reduce heat transfer to the base; (8) base attached to SEM motorized stage; (9) a convoluted tube attached to the base containing the LN_2 and electronic connectors. Panel B: The IN-ESEM system consists of: an ESEM chamber (indicated as a dashed square), temperature control unit (shown on the left), and a water vapor source (shown to the right of the ESEM chamber) providing a flow of humidified N_2(g).

A temperature sensor (±0.15 K, Pt-100, Omega Engineering Inc.) embedded below the sample holder is calibrated, as described below, to monitor the sample temperature.

To perform ice nucleation experiments as a function of RH it is critical that the observed sample area is the coldest spot in the entire setup. Otherwise, water diffuses to the coldest point and results in ice buildup at unwanted locations, ultimately disrupting the experiment. Furthermore, the gradient of water vapor in the chamber is altered during the experiment; this results in uncertainty in the RH above the sample (which is derived from the known water partial pressure and sample temperature). To circumvent these effects, the cryo-cooling stage is placed into an evacuated housing assembly mounted in the ESEM chamber. The liquid nitrogen supply tubes and electronic connectors are also contained within the evacuated assembly (Fig. 1). Additionally, to ensure that this tube does not act as a cryo-pump for gases in the ESEM chamber, its exterior is wrapped with heating tape. To minimize water adsorption, the cover and base of the ice nucleation cell are made out of high-density polyether ether ketone (PEEK). These efforts are to ensure that the sample area is the coldest part in the system.

Fig. 1B shows the schematic of the IN-ESEM platform assembly with the IN cell installed inside the ESEM chamber. The IN-ESEM system is interfaced with a temperature control unit (Model 22C, Cryogenic Control Systems, Inc.) and a water vapor supply setup. The field emission gun ESEM (Quanta 3D model, FEI, Inc.) with a gaseous secondary electron detector is used for imaging. The ESEM is equipped with imaging software to continuously monitor and record *in situ* changes over the sample. At the lowest magnification, the entire 0.2 mm^2 sample area is within the image frame, which is digitally recorded. The temperature control unit regulates the power output for the heating element based upon the temperature sensor reading. The water vapor source provides water vapor for inducing ice nucleation and for imaging in ESEM. For the ESEM used in this study, the adaptable chamber pressure ranges from 10 Pa to 2600 Pa. In general, the spatial resolution of the microscope is decreased at higher pressures, thus only water vapor was used at temperature above 230 K to achieve better spatial resolution for the imaging. Because of the minimum chamber pressure of 10 Pa, the mixture of N_2 and water vapor is used to achieve lower dew points (*i.e.*, Saturation water vapor partial pressure less than 10 Pa) for the ice nucleation temperature below 230 K. Total operating pressures in the ESEM range between 10–600 Pa. These low operating pressure conditions can cause the volatilization of semivolatile materials from particles which could affect the particle physiochemical properties. Thus, IN-ESEM measurements need to be assessed with this caveat in mind. Ultra-high purity dry N_2(g) passes through a temperature controlled water reservoir and mixes with additional dry N_2(g) to set a desired dew point, (T_d), and then is pumped into the ESEM chamber. The water vapor partial pressure in the chamber is varied by changing the temperature of the water reservoir and the N_2(g) flows. The water vapor partial pressure is inferred from the measurement of T_d using a chilled mirror hygrometer (GE Sensing, Model 1311XR) operating over 188–303 K. The flow of humidified N_2(g) is ~0.5 standard liter per minute.

2.2 Particle sample generation and collection

Laboratory generated particles of kaolinite (Fluka), NaCl (Sigma-Aldrich, >99%), and a sample of field-collected ambient particles were used. Silicon wafer substrates coated with a silicon nitride film (Silson Ltd, for the remainder of the manuscript referred to as the substrate) were used. Kaolinite particles used for ice nucleation experiments and helium ion microscope imaging were dry deposited onto the substrate as described in previous studies.[39] The deposited kaolinite particle diameters were less than 10 μm, with a mean diameter of 2–3 μm as determined from SEM images. NaCl particles were generated by nebulizing 0.5 M NaCl aqueous solution, the aerosols pass through a diffusion dryer, and are collected by a cascade Multi Orifice Uniform Deposition Impactor (MOUDI).[40] NaCl particles were collected at the 7th stage of the MOUDI with a 50% cut-off aerodynamic diameter of 0.56 μm. The ambient particle sample was collected with a MOUDI (8th stage with 50% cut-off diameter of 0.32 μm) at the ground sampling site during the California Research at the Nexus of Air Quality and Climate Change (CalNex) campaign on May 19, 2010 (12 am to 6 am).[20]

2.3 Experimental procedure and INP identification

Two types of ice nucleation experiments are possible with the IN-ESEM system: (i) isobaric ice nucleation experiments at a constant water partial pressure (*i.e.* the dew point temperature (T_d) is constant), while the temperature of a sample/particles (T_p) decreases, thereby simulating cloud formation in the atmosphere; (ii) isothermal ice nucleation experiments where T_p is kept constant and the water vapor partial pressure is increased to increase RH_{ice}. The isobaric experiments are performed to detect ice nucleation onsets for an ensemble of particles present in the entire sample (~0.2 mm^2 sample area) at the low magnification of ESEM, followed by subsequent tracking and chemical imaging of individual INPs. The isobaric experiments serve to yield the ice nucleation ability of the sample. Individual sub-micrometer size particles are usually not clearly seen at the first part of the experiment when the ice nucleation onsets are recorded at coarse magnification. The second part of the experiment involves tracking and detailed imaging of individual INPs. The isothermal ice nucleation experiments are performed at selected temperatures, whereas water vapor partial pressure is gradually increased at the rate of ~15 Pa min^{-1} starting from 10 Pa. In these experiments, ice nucleation events on individual particles are imaged with high magnification. Both isobaric and isothermal experiments can be conducted for ice nucleation onset measurements, ice nucleating particle tracking, and ice nucleation location tracking.

Fig. 2 illustrates the experimental trajectories of RH_{ice} *versus* T_p in the isobaric ice nucleation experiments. First, T_p is decreased from room temperature at a rate of about 2–5 K min^{-1} to the investigated temperature (a few degrees higher than T_d). Then, the water vapor partial pressure in the ESEM chamber is adjusted to reflect sub-saturation, $RH_{ice} < \sim 90\%$, as illustrated by the blue square in Fig. 2. Subsequently, T_p is decreased (at a selected rate of 0.2–0.5 K min^{-1}) to increase RH_{ice} until

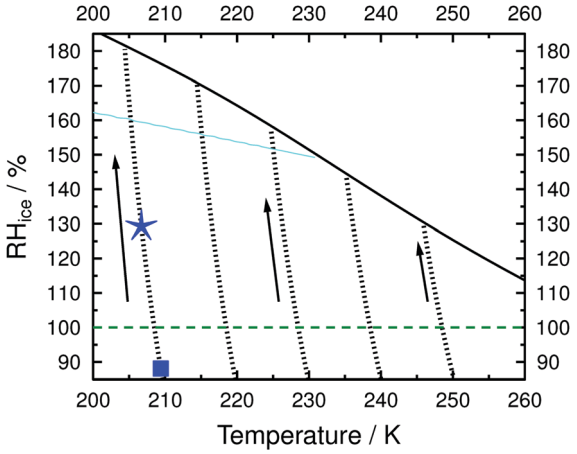

Fig. 2 Representative experimental RH_{ice} *versus* particle temperature (T_p) trajectories (dotted black lines) for the isobaric experiments. The black solid, green dashed, and cyan solid lines represent water saturation (RH_w = 100%), ice saturation (RH_{ice} = 100%), and homogeneous ice nucleation limit, respectively.[41] Arrows indicate the increase of RH_{ice} along the trajectories. The square symbol indicates the starting point of an experiment and the star indicates the observed onset of an ice nucleation event.

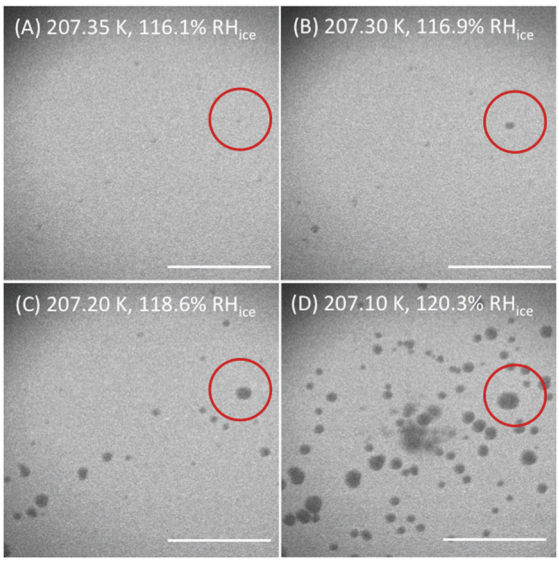

Fig. 3 Ice nucleation on kaolinite particles imaged by IN-ESEM. Images show (A) before ice formation, small gray dots depict the kaolinite particles; (B) first ice nucleation event (onset), the first ice crystals become visible (circle); and (C and D) more ice crystals form after increase in RH_{ice}. T_p and RH_{ice} are shown in the legends. Scale bars are 100 μm.

formation of ice or water uptake is observed (indicated by the blue star in Fig. 2). Consecutive ESEM images are acquired every 3 seconds. During each experiment, the electron beam exposure is minimized by using (1) a short scanning time (*i.e.*, 1–3 μs per line), (2) low number of lines (512 or 1024 lines per frame), and (3) lower electron beam current (*i.e.*, less than 0.43 nA) to reduce potential beam damage. At these settings the temperature of the sample changes no more than 0.025 K during image acquisition time. T_p and total pressure in the chamber are recorded continuously. After observation of an ice nucleation event, T_d is calibrated as described in Section 2.4. RH_{ice} over the particles is calculated from the calibrated T_d and T_p according to $RH_{ice} = P(T_d)/P_{ice}(T_p)$ where $P(T_d)$ and $P_{ice}(T_p)$ represent the water vapor partial pressure in the ESEM chamber and the saturation vapor pressure over ice at T_p, respectively.[41]

The onsets of ice formation (or water uptake) by particles are determined by the changes in particle size (or phase) from the recorded ESEM images. With a lateral resolution of ~50 nm, very small amounts of liquid water on the particles (from water vapor condensation) can be detected by ESEM imaging. The ice nucleation onset is defined as the value of T_p and RH_{ice} where initial ice formation or water uptake is observed. Ice formation following the water uptake is determined as immersion (or condensation) freezing. Deposition ice nucleation occurred when no visible liquid water uptake was evident in the ESEM images. Fig. 3 and Movie S1 (ESI†) illustrate examples of deposition ice nucleation and immersion freezing induced by kaolinite particles, respectively. Fig. 3 displays a selected set of images of deposition ice nucleation recorded in an isobaric experiment. Starting at 210 K, the particle temperature was decreased at 0.5 K min^{-1} and images were recorded every 3 seconds. As shown in Fig. 3, the ice nucleation onset on kaolinite particles occurred at 207.3 K and 116.9% RH_{ice}. After the first ice nucleation event, the particle temperature continuously decreased, resulting in a continuous increase of RH_{ice} during which additional ice nucleation events proceeded. For identification of INPs after ice crystal formation, the sample was warmed at a rate of 0.5–4 K min^{-1} while images were recorded until the ice crystals completely sublimate and only the residual INPs remained. Movie S2 (ESI†) shows an example of the INP identification process which is discussed below.

2.4 Precise temperature measurements

For precise measurements of sample temperature and RH_{ice} calculation, T_p and T_d require accurate calibration. T_p was calibrated by measuring the melting points of three standards: 1-hexanol (221.15 K), decane (243.55 K), and dodecane (263.58 K) purchased from Sigma-Aldrich (99% purity). For each compound, the measurement was repeated a minimum of 6 times employing three independent samples as described previously.[38] The calibration confirmed that the response of the temperature sensor embedded in the cryo-stage was linear from 190–273 K with an uncertainty less than 0.2 K (see Fig. S1 and Movie S3, ESI†).

The water vapor partial pressure inside the ESEM chamber, $P(T_d)$, is determined by measuring the 2-D projected surface area (SA) of ice crystals as T_p was varied.[39] With a constant $P(T_d)$ in the chamber ice crystals grow or shrink (*i.e.* their SA increases or decreases, respectively) by decreasing or increasing the sample temperature T_p below or above T_d, respectively. Fig. 4 and Movie S4 (ESI†) illustrate the T_d calibration experiment. At the beginning of the calibration experiment with an ice crystal present, T_p is higher than T_d ($RH_{ice} < 100\%$), resulting in sublimation of the ice crystal and a corresponding decrease in SA. At equilibrium, the ice crystal maintains a constant SA reflecting $T_p = T_d$ ($RH_{ice} = 100\%$). Further decreasing of T_p results in growth of the ice crystal *via* water vapor deposition.

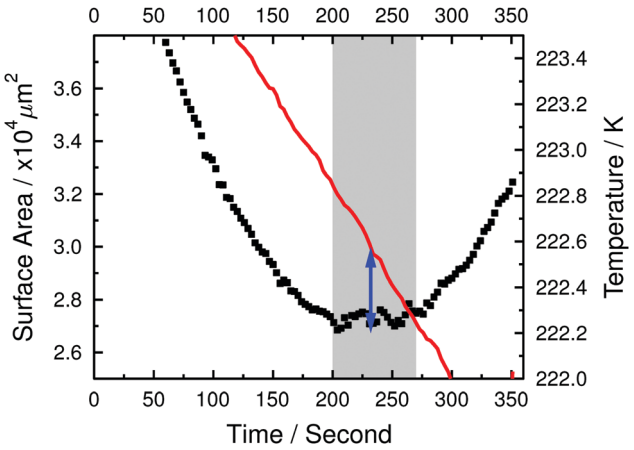

Fig. 4 Changes in ice crystal surface area (black symbols) and temperature (solid red line) during a dew point temperature (T_d) calibration experiment.[39] The blue arrow and gray area indicate the equilibrium point when T_d equals T_p of the ice crystal (RH_{ice} = 100%) resulting in the minimum ice crystal surface area.

The resulting conservative experimental uncertainties are $\Delta T_p < \pm 0.2$ K, $\Delta T_d < \pm 0.25$ K, $\Delta RH_{ice} < \pm 11\%$ at 200 K, and $\Delta RH_{ice} < \pm 3\%$ at 260 K. In addition to the T_p and T_d calibration, the observed deliquescence of NaCl particles (DRH = 78% at 252 K) was in excellent agreement with previous reports.[42,43] As shown in Movie S5 (ESI†), both NaCl deliquescence and water condensation occurred uniformly across the sample area, indicating homogeneous water vapor distribution across the 0.2 mm^2 sample area probed in the experiments presented here.

2.5 Chemical imaging of individual INP

Identified INPs were characterized by micro-spectroscopic analyses using scanning electron microscopy with energy dispersed analysis of X-rays (SEM/EDX) and scanning transmission X-ray microscopy with near edge X-ray absorption fine structure spectroscopy (STXM/NEXAFS). ESEM, equipped with an EDAX X-ray spectrometer with a Si(Li) detector with a 10 mm^2 active area and an ATW2 window, was used to determine the size, surface area, morphology, and elemental composition of individual particles including the INPs.[19–21] X-ray analysis of the identified INPs was acquired at an acceleration voltage of 20 kV and a beam current of 430 pA. Elemental compositions of INPs were determined from the recorded X-ray spectra. More details on the SEM/EDX analysis and X-ray mapping of individual particles are reported elsewhere.[44,45] Individual INP characterization at high resolution was always performed after ice nucleation experiments to minimize potential beam damage from extended electron beam exposure.

Digital pattern records allowed relocation of INPs in separate single-particle analysis by STXM/NEXAFS.[21] STXM/NEXAFS has been applied in numerous studies of atmospheric particles. An overview of the application of this technique and analysis of particles and technical details are published elsewhere.[46–50] STXM/NEXAFS detects transmitted soft X-rays generated from the synchrotron light source across a raster-scanned sample. Images are obtained over a range of photon energies to provide NEXAFS spectra.[51] Analysis of NEXAFS spectra provide chemical composition and mixing states of individual particles with spatial resolution of ~30 nm.[52–56] Acquired carbon K-edge spectra allow identification of the organic carbon, elemental carbon (*i.e.* soot), and overall contribution of inorganic components within individual particles.

A helium ion microscope (HeIM, Orion NanoFab, Zeiss Inc.), a surface sensitive technique,[57] was used for advanced imaging of the surface ultrastructure of particles. The instrument was operated at 30 keV and 1.0 pA with a spatial resolution of 0.8 nm. The HeIM imaging revealed ultrastructural details and surface topography of kaolinite particles.

3. Results and discussion

3.1 Isobaric ice nucleation experiments

Evaluation of the IN-ESEM platform performance was conducted by measuring ice nucleation onsets of blank substrates and standard kaolinite particles in isobaric ice nucleation experiments.[39] Ice nucleation on the substrate (in the absence of particles) was performed to determine the onset conditions of ice nucleation induced by the substrate itself. Fig. 5 shows water condensation on the blank substrate at water saturation (RH_w = 100%) corresponding to RH_{ice} from 120% to 145% for temperatures from 255 to 235 K. Below 235 K, ice nucleation occurred on the substrates at RH_{ice} from 148% to 165%. These results are consistent with our previous measurements on the same substrates using the OM technique.[19,21,39]

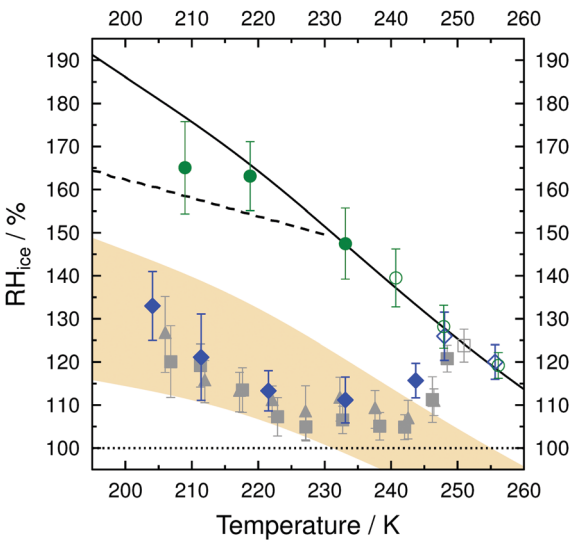

Fig. 5 Ice nucleation onsets detected in IN-ESEM experiments over kaolinite particles and particle-free substrates. Solid, dotted, and dashed lines indicate the water saturation (RH_w = 100%), ice saturation, and homogeneous ice nucleation limit,[65] respectively. Green solid and open circles indicate the onsets of ice nucleation and water condensation on a blank substrate, respectively. Symbols represent the ice nucleation onsets of kaolinite particles using IN-ESEM system (blue diamonds) and optical microscopy method (various grey symbols)[19,39] *via* immersion freezing (open symbols) and deposition mode (solid symbols), respectively. Light brown shaded area indicates the suggested conditions[66] required for homogeneous ice nucleation in 7.5–15 nm pores.

The measurements on the particle-free substrates indicate the range in T_p and RH_{ice} below which the substrate has no effect on ice nucleation.

Fig. 5 and Fig. S2 (ESI†) compare the ice nucleation onsets of kaolinite particles detected in these IN-ESEM experiments to previous studies.[19,39,58–64] In this study, the total particle surface areas available for the ice nucleation ($0.5–2.6 \times 10^{-2}$ mm^2) were about a factor of three lower than those used previously ($1.3–7.9 \times 10^{-2}$ mm^2).[19,39] The results obtained using the IN-ESEM system are in excellent agreement with previously reported data.[39] Below 246 K, kaolinite particles initiated ice nucleation through the deposition mode (*i.e.*, no liquid water involved). The results show that the RH_{ice} onset required for ice nucleation on kaolinite particles decreased from 115.7% RH_{ice} at 244 K to a lower onset of 111.2% RH_{ice} at 233 K, and then continuously increased to 133% RH_{ice} at 204 K. Above 246 K, first water condensed on the particles which was followed by immersion freezing at water saturation conditions. Previous studies reported the lowest temperature for immersion freezing ranged between 251 and 254 K[31,39,58,64] in agreement with this study. The high-resolution imaging capability of IN-ESEM revealed water condensation on kaolinite particles at temperatures as low as 246 K demonstrating the ability to discriminate between different ice nucleation pathways.

3.2 Isothermal ice nucleation experiments

Identifying the nucleation sites or locations within individual particles or substrate surface is essential for obtaining a fundamental understanding of heterogeneous ice nucleation. There are no reports of direct experimental detection of heterogeneous ice nucleation at the nanoscale.[67–69] It has been suggested that morphological features on mineral surfaces, such as steps, cracks, and cavities promote ice nucleation.[67] Fig. 6 shows the typical morphology of kaolinite particles imaged by HeIM. The kaolinite particles have layered structures of stacked platelets oriented perpendicular to their basal planes.[70–73] The surfaces of the basal planes are relatively smooth (Fig. 6E–H), whereas edge surfaces of the stacked platelets are much rougher (Fig. 6A–D). Roughness of particles surfaces can be assessed through digital processing of the gray scale intensity of HeIM images which reflect the secondary electron signal from the surface. Adjacent peaks of the grayscale intensities along a line scan over the HeIM image indicate surface irregularities, such as steps, cracks, or trenches, and the distances between these peaks indicate the sizes of these irregularities (see Fig. 6C and G). Characterization of kaolinite particles using HeIM imaging indicates that the trenches along the stacked platelets range from 30 to 110 nm with a mode size of ~55 nm, whereas the surface irregularities on the basal plane range from a few nanometers to 20 nm with a mode of ~9 nm. These observations are consistent with previously reported values.[71,74–76]

The IN-ESEM platform provides the capability to identify the location of ice nucleation events within individual particles and is capable of capturing early stages of ice formation and its dynamic evolution. Fig. 7 demonstrates dynamic imaging of ice micro-crystals formed on a kaolinite particle. This isothermal ice nucleation experiment was performed at 205.4 K and water partial pressure starting at 10 Pa increasing at the rate of ~15 Pa min^{-1} (*i.e.*, RH_{ice} increases at the rate of ~3% min^{-1}). ESEM images in Fig. 7 display the location of ice nucleation events on an individual particle followed by growth of the hexagonal ice crystals. As shown in the images, ice crystals nucleate on the side of the stacked platelets, rather than on their basal planes. At these experimental conditions, ice nucleation is likely not occurring on

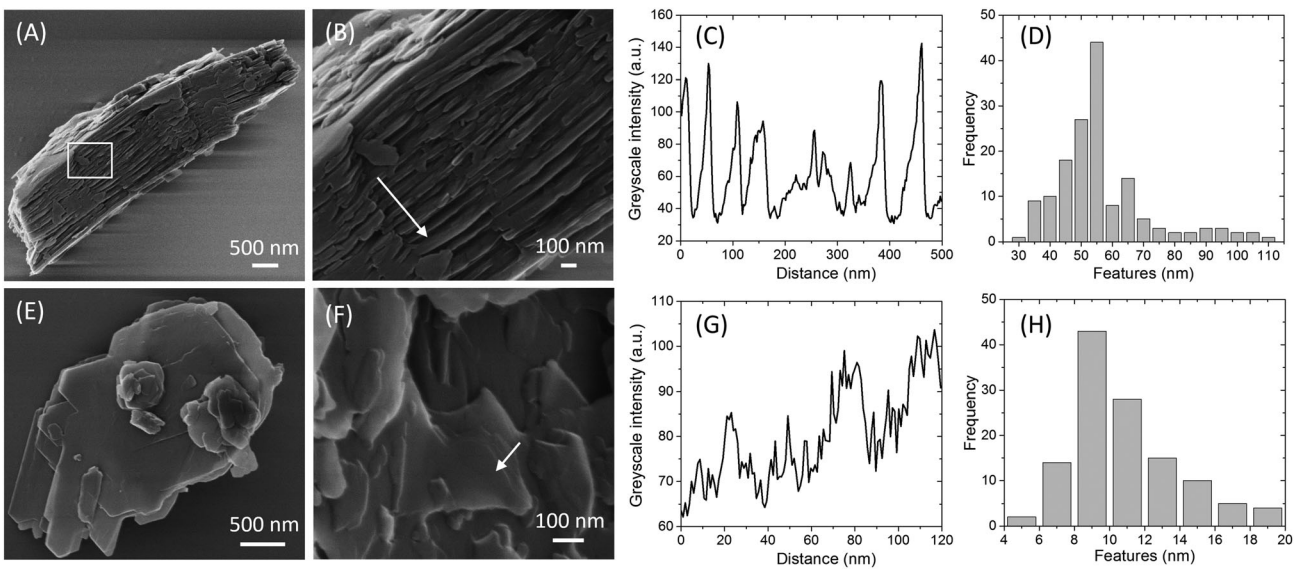

Fig. 6 Characteristic surface irregularities of kaolinite particles, such as steps, cracks, or trenches. (A, B, E and F) HeIM images showing surface morphology of kaolinite particles, panel B shows an enlarged image for the marked area in panel A. (C and G) Surface roughness expressed as grayscale intensities for the line scans along the arrows marked in panels B and F, respectively. The gray values are used to infer characteristic sizes of surface features summarized by the size distribution histograms (D and H).

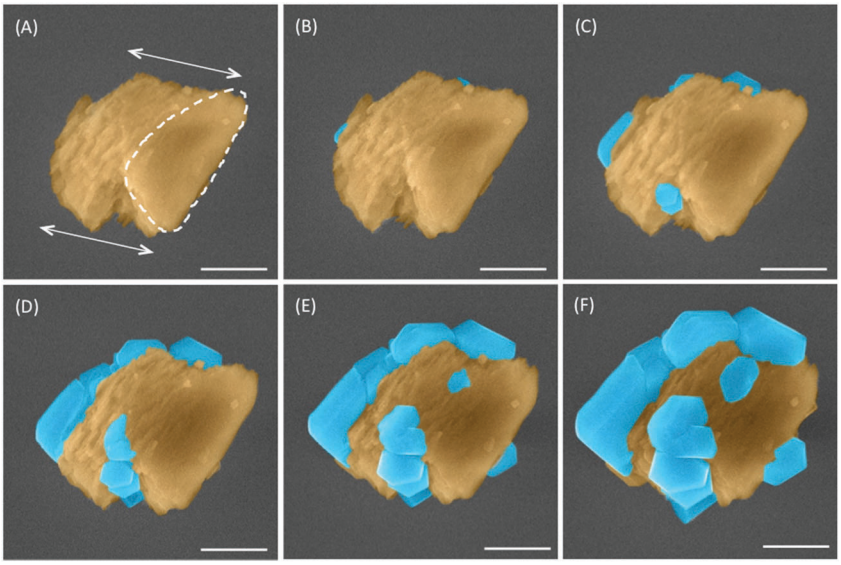

Fig. 7 Isothermal nucleation of ice on an individual kaolinite particle at 205.4 K. Ice formation is initiated at 124 Pa. False-colored images of kaolinite (brown) and ice crystals (blue) are shown for clarity. Dashed contour line shows the basal plane and arrows indicate direction of the stacked kaolinite platelets. Images show (A) prior to ice nucleation; (B) onset of ice formation, 124.2% RH_{ice}; (C–F) post ice nucleation event and growth of the ice crystals. ESEM images A–F were acquired sequentially, separated by 3 seconds. Scale bars are 5 μm.

the basal planes present within the stacked layers because no nucleation is initiated on the outermost basal plane which is directly exposed to water vapor in the ESEM chamber. Thus, the edges of the stacked platelets are responsible for the formation of ice which was consistently observed here. This observation was further confirmed by additional isothermal experiments included in Fig. S4 and S5 of the ESI.†

Recently, it was proposed that deposition ice nucleation on mineral surfaces was likely a homogeneous or immersion freezing of water in pores or cavities.[66] Experimentally derived onset conditions shown in Fig. 5 are compared to modeled predictions of pore condensation and freezing (PCF) onsets.[66] Fig. 5 includes the calculated PCF freezing onsets for pore sizes in the ranges of 7.5–15 nm as the light brown colored area. The majority of deposition ice nucleation onsets for temperatures lower than 245 K fall in the range in which homogeneous freezing in 7.5–15 nm pores is expected. As discussed above, the surface irregularities on the basal planes of kaolinite range from a few nanometers to 20 nm with a mode of ~9 nm. These surface irregularities are in general agreement with the estimated pore sizes for underlying PCF calculations. Assuming that ice nucleated by homogenous freezing of water in ~9 nm pores on the particle surface, some ice nucleation events should have also been observed on the basal planes. However, based on closer examination of multiple isothermal experiments on individual kaolinite particles, (Fig. 7, Fig. S4 and S5, ESI†), formation of ice was consistently observed only on the edges of the stacked platelets. These cannot be fully explained by the PCF hypothesis. These observations suggest that likely chemical differences between the edge and the basal plane surfaces may define their propensity to nucleate ice. The kaolinite surfaces consist of either hydroxylated alumina or non-hydroxylated siloxane basal planes of the platelets held together by hydrogen bonding. The platelets' edges are terminated with dangling OH groups that can be protonated or unprotonated.[36,68,77] Theoretical chemistry modeling has shown that the edges of kaolinite particles have a stronger affinity for water and both protonated and unprotonated edges would absorb water at lower RH than alumina and siloxane basal planes.[36] Our experimental observations suggest that the edges of platelets are the active sites of ice formation on kaolinite particles. Although hexagonal rings of water molecules are not predicted to form on the edges of kaolinite,[77] different forms of ice might have nucleated at the early stage and then transformed into the thermodynamically favorable hexagonal ice.[36,78] Further simulation study is needed to confirm this hypothesis.

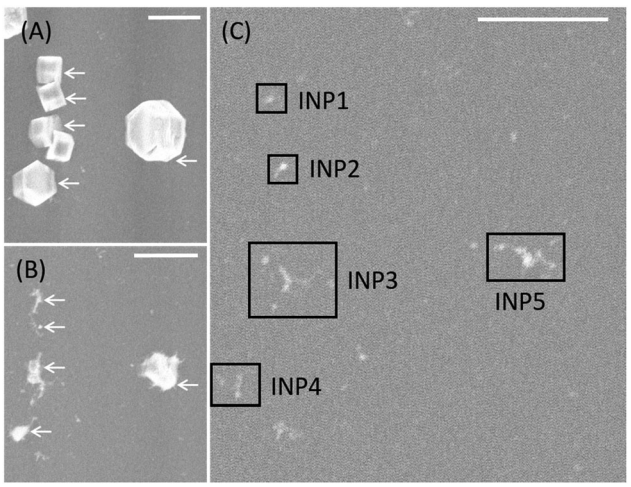

Fig. 8 Identification of individual INPs. (A) Ice crystals nucleated on the particles; (B) sublimation of ice crystals; (C) identification of INP (in black squares) after complete sublimation. Scale bars are 10 μm.

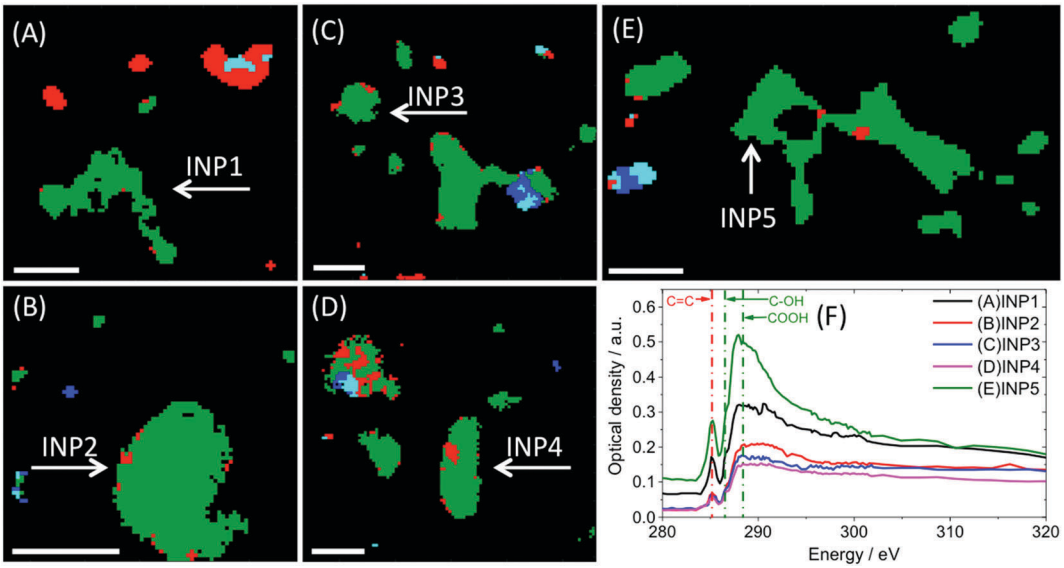

Fig. 9 Chemical imaging of individual INPs using STXM/NEXAFS analysis. (A–E) The compositional maps of individual particles including the INPs (marked by arrows). The different colors represent organic carbon (green), organics and inorganics (blue), organics and elemental carbon (red), and a mixture of organic, elemental carbon and inorganics (cyan).[50] (F) Carbon K-edge spectra for the five identified INPs. The absorption bands of 285.4, 288.5 eV, and 286.5 eV are also shown. Scale bars are 1 μm.

3.3 Chemical imaging of individual atmospheric INPs

To demonstrate the experimental capability of tracking and chemical imaging of micrometer or sub-micrometer size INPs, ice nucleation experiments were also conducted on particles collected during the CalNex field campaign. In an experiment mimicking cirrus cloud conditions, a group of INPs initiated ice nucleation at ~145.3% RH_{ice} and 205.4 K *via* deposition mode. The onset values are consistent with our previous OM observations over particles collected at the same location, time, and with similar total particle surface areas for ice nucleation (0.15 *vs.* 0.26 mm^2).[20] Fig. 8 illustrates the identification of the INPs in the field-collected sample. Fig. 8A and B display the sublimation of ice crystals. Once the ice crystal completely sublimates, it leaves behind the INP residues as shown in Fig. 8C. Movie S5 (ESI†) shows the dynamic sublimation of these ice crystals.

The sample with identified INPs was transferred for STXM/NEXAFS analysis which was then followed by SEM/EDX elemental analysis. STXM/NEXAFS allows characterization of the carbon bonding and the mixing states of individual INPs. Carbon K-edge spectra were collected for the selected sample areas including the identified INPs and particles in close proximity to the INPs which did not nucleate ice. Fig. 9A–E show the compositional maps of five selected sample areas. The compositional maps illustrate the spatial distribution of major carbon-type components within individual particles. This analysis demonstrates that INPs in the selected sample were composed of organic and elemental carbon. These results are consistent with the SEM/EDX analysis showing that these INPs only contain C, N, O as illustrated in Fig. S3 (ESI†).

Fig. 9 indicates that the composition and mixing states of the identified INP are similar to those of the surrounding non-nucleating particles. The STXM/NEXAFS analysis demonstrates the complex composition of the INPs. The relative contributions of chemical components of the identified INPs are different. Based on the Carbon K-edge spectra shown in Fig. 9F, the optical density at the characteristic energy for different carbon functional groups, such as COOH (288.5 eV) and C=C (285.4 eV), shows the abundance of different organic species within the individual INPs.[50] Every INP differs somewhat in terms of its composition, morphology, and mixing state, although the overall composition is similar among those particles. Thus, the combination of complementary analytical techniques can advance the fundamental understanding of ice nucleation by these ambient particles. The ice nucleation measurement observed in the IN-ESEM experiments combined with chemical imaging by SEM/EDX and STXM/NEXAFS allows in-depth physical and chemical characterization of individual INP and has the potential to yield physicochemical picture of heterogeneous ice nucleation.

4. Conclusions

The novel IN-ESEM experimental platform was employed to investigate ice nucleation by laboratory generated and atmospheric particles at temperatures and RH relevant for cloud formation. The IN-ESEM system was calibrated by measuring the melting points of organic compounds and validated using ice nucleation onset measurements on kaolinite particles. A field collected particle sample was used to illustrate the identification and chemical imaging of sub-micrometer size INPs. The IN-ESEM platform can be applied to microscopic observation of individual ice formation events, detection of freezing temperatures and RH onsets, and identification and location of ice crystals on particle surfaces. When complemented by chemical imaging techniques, the IN-ESEM ice nucleation

measurements allow the physicochemical description of INPs. The IN-ESEM experiments allow ice nucleation examination with precise control of temperature and RH at atmospherically relevant ranges. The location of ice crystals on the particle surfaces that initiate ice nucleation can be detected with a lateral resolution of ~10 nm. Isothermal ice nucleation experiments on individual kaolinite particles have shown that ice preferably nucleates on the edges of the stacked kaolinite platelets, and not on their basal planes. These experimental observations indicate that the OH terminated edge surfaces of kaolinite platelets are potential ice nucleation sites. The chemical differences between the edge and the basal plane surfaces might have contributed to their different propensities to nucleate ice. Theoretical chemistry simulations of ice nucleation on both the edge and the basal plane surfaces are necessary to provide further insights.

IN-ESEM is ideally suited to study ice crystal growth and morphology under a wide range of thermodynamic conditions.[79–81] Phase transitions[82,83] for inorganic and organic materials can be investigated *in situ* in great detail and under very low temperatures. The IN-ESEM platform can also be applied to other research areas where well-controlled temperature or RH are required such as cryobiology.[1–3] The IN cell and associated control units are modular and can be implemented in other analytical instrumentation such as a Raman or Fourier transform infrared microscope to investigate the interaction of ice or water with other materials.[84] The sample holder can be readily modified to suit different samples/substrate sizes. In general, the IN-ESEM platform provides a new experimental tool to probe effects on the nanoscale of various materials in response to low temperatures and concomitant variation in RH with previously unachieved precision and resolution. This technique opens a pathway to new physical chemistry endeavors to study ice formation processes relevant to atmospheric science, cryobiology, and material science.

Acknowledgements

PNNL group acknowledges support by Laboratory Directed Research and Development funds of Pacific Northwest National Laboratory (PNNL). D. A. K. acknowledges support by the U.S. Department of Energy, Office of Science (OBER), under Award Number DE-SC0016370. M. K. G. acknowledges support from the Condensed Phase Interfacial Molecular Science Program of the Department of Energy Basic Energy Sciences. PNNL is operated by the U.S. DOE by Battelle Memorial Institute under contract DE-AC06-76RL0. The ESEM imaging and SEM/EDX particle analysis were performed in the Environmental Molecular Sciences Laboratory, a national scientific user facility sponsored by OBER at PNNL. The STXM/NEXAFS particle analysis was performed at beamlines 11.0.2 and 5.3.2 at the Advanced Light Source (ALS) at Lawrence Berkeley National Laboratory. The work at the ALS was supported by the Director, Office of Science, Office of Basic Energy Sciences, of the U.S. DOE under Contract No. DE-AC02-05CH11231.

References

1 G. J. Morris and E. Acton, *Cryobiology*, 2013, **66**, 85–92.
2 R. E. Lee and J. P. Costanzo, *Annu. Rev. Physiol.*, 1998, **60**, 55–72.
3 J. O. M. Karlsson and M. Toner, *Biomaterials*, 1996, **17**, 243–256.
4 B. Li and D. W. Sun, *J. Food Eng.*, 2002, **54**, 175–182.
5 O. Parent and A. Ilinca, *Cold Reg. Sci. Technol.*, 2011, **65**, 88–96.
6 F. T. Lynch and A. Khodadoust, *Prog. Aerosp. Sci.*, 2001, **37**, 669–767.
7 D. A. Hegg and M. B. Baker, *Rep. Prog. Phys.*, 2009, **72**, 056801.
8 B. A. Albrecht, *Science*, 1989, **245**, 1227–1230.
9 M. B. Baker, *Science*, 1997, **276**, 1072–1078.
10 J. P. D. Abbatt, S. Benz, D. J. Cziczo, Z. Kanji, U. Lohmann and O. Möhler, *Science*, 2006, **313**, 1770–1773.
11 G. Vali, P. J. DeMott, O. Möhler and T. F. Whale, *Atmos. Chem. Phys.*, 2015, **15**, 10263–10270.
12 M. Ebert, M. Inerle-Hof and S. Weinbruch, *Atmos. Environ.*, 2002, **36**, 5909–5916.
13 R. C. Hoffman, A. Laskin and B. J. Finlayson-Pitts, *J. Aerosol Sci.*, 2004, **35**, 869–887.
14 N. Hiranuma, S. D. Brooks, B. W. Auvermann and R. Littleton, *Atmos. Environ.*, 2008, **42**, 1983–1994.
15 R. E. O'Brien, B. Wang, S. T. Kelly, N. Lundt, Y. You, A. K. Bertram, S. R. Leone, A. Laskin and M. K. Gilles, *Environ. Sci. Technol.*, 2015, **49**, 4995–5002.
16 J. L. Hand, W. C. Malm, A. Laskin, D. Day, T. Lee, C. Wang, C. Carrico, J. Carrillo, J. P. Cowin, J. Collett and M. J. Iedema, *J. Geophys. Res.: Atmos.*, 2005, **110**, D21210.
17 A. Laskin, M. J. Iedema, A. Ichkovich, E. R. Graber, I. Taraniuk and Y. Rudich, *Faraday Discuss.*, 2005, **130**, 453–468.
18 A. Laskin, T. W. Wietsma, B. J. Krueger and V. H. Grassian, *J. Geophys. Res.: Atmos.*, 2005, **110**, D10208.
19 D. A. Knopf, B. Wang, A. Laskin, R. C. Moffet and M. K. Gilles, *Geophys. Res. Lett.*, 2010, **37**, L11803.
20 B. B. Wang, A. Laskin, T. Roedel, M. K. Gilles, R. C. Moffet, A. V. Tivanski and D. A. Knopf, *J. Geophys. Res.: Atmos.*, 2012, **117**, D00V19.
21 D. A. Knopf, P. A. Alpert, B. Wang, R. E. O'Brien, S. T. Kelly, A. Laskin, M. K. Gilles and R. C. Moffet, *J. Geophys. Res.: Atmos.*, 2014, **119**, 10365–10381.
22 Z. A. Kanji and J. P. D. Abbattt, *J. Phys. Chem. A*, 2010, **114**, 935–941.
23 K. J. Baustian, D. J. Cziczo, M. E. Wise, K. A. Pratt, G. Kulkarni, A. G. Hallar and M. A. Tolbert, *J. Geophys. Res.: Atmos.*, 2012, **117**, D06217.
24 G. P. Schill and M. A. Tolbert, *J. Phys. Chem. C*, 2014, **118**, 29234–29241.
25 S. K. Sihvonen, G. P. Schill, N. A. Lyktey, D. P. Veghte, M. A. Tolbert and M. A. Freedman, *J. Phys. Chem. A*, 2014, **118**, 8787–8796.
26 D. A. Knopf and T. Koop, *J. Geophys. Res.: Atmos.*, 2006, **111**, D12201.

27 P. J. DeMott, D. C. Rogers and S. M. Kreidenweis, *J. Geophys. Res.: Atmos.*, 1997, **102**, 19575–19584.
28 D. C. Rogers, P. J. DeMott, S. M. Kreidenweis and Y. L. Chen, *Geophys. Res. Lett.*, 1998, **25**, 1383–1386.
29 B. Kärcher and J. Strom, *Atmos. Chem. Phys.*, 2003, **3**, 823–838.
30 B. Kärcher and U. Lohmann, *J. Geophys. Res.: Atmos.*, 2003, **108**, 4402.
31 F. Zimmermann, M. Ebert, A. Worringen, L. Schütz and S. Weinbruch, *Atmos. Environ.*, 2007, **41**, 8219–8227.
32 F. Zimmermann, S. Weinbruch, L. Schütz, H. Hofmann, M. Ebert, K. Kandler and A. Worringen, *J. Geophys. Res.: Atmos.*, 2008, **113**, D23204.
33 N. B. Magee, A. Miller, M. Amaral and A. Cumiskey, *Atmos. Chem. Phys.*, 2014, **14**, 12357–12371.
34 B. J. Fuller, *CryoLetters*, 2004, **25**, 375–388.
35 T. Croteau, A. K. Bertram and G. N. Patey, *J. Phys. Chem. A*, 2008, **112**, 10708–10712.
36 T. Croteau, A. K. Bertram and G. N. Patey, *J. Phys. Chem. A*, 2010, **114**, 8396–8405.
37 T. Croteau, A. K. Bertram and G. N. Patey, *J. Phys. Chem. A*, 2010, **114**, 2171–2178.
38 D. A. Knopf and M. D. Lopez, *Phys. Chem. Chem. Phys.*, 2009, **11**, 8056–8068.
39 B. Wang and D. A. Knopf, *J. Geophys. Res.: Atmos.*, 2011, **116**, D03205.
40 B. Wang, R. E. O'Brien, S. T. Kelly, J. E. Shilling, R. C. Moffet, M. K. Gilles and A. Laskin, *J. Phys. Chem. A*, 2015, **119**, 4498–4508.
41 D. M. Murphy and T. Koop, *Q. J. R. Meteorol. Soc.*, 2005, **131**, 1539–1565.
42 D. J. Cziczo and J. P. D. Abbatt, *J. Phys. Chem. A*, 2000, **104**, 2038–2047.
43 T. Koop, A. Kapilashrami, L. T. Molina and M. J. Molina, *J. Geophys. Res.: Atmos.*, 2000, **105**, 26393–26402.
44 A. Laskin, in *Fundamentals and Applications in Aerosol Spectroscopy*, ed. R. Signorell and J. Reid, Taylor and Francis Books, Inc., 2010, pp. 463–491.
45 A. Laskin, J. P. Cowin and M. J. Iedema, *J. Electron Spectrosc. Relat. Phenom.*, 2006, **150**, 260–274.
46 S. Ghorai, A. Laskin and A. V. Tivanski, *J. Phys. Chem. A*, 2011, **115**, 4373–4380.
47 S. Ghorai and A. V. Tivanski, *Anal. Chem.*, 2010, **82**, 9289–9298.
48 R. C. Moffet, A. V. Tivanski and M. K. Gilles, in *Fundamentals and Applications in Aerosol Spectroscopy*, ed. R. Signorell and J. P. Reid, Taylor and Francis Books, Inc., 2010, pp. 419–462.
49 M. K. Gilles, R. C. Moffet and A. Laskin, *Geochim. Cosmochim. Acta*, 2010, **74**, A332–A332.
50 R. C. Moffet, T. Henn, A. Laskin and M. K. Gilles, *Anal. Chem.*, 2010, **82**, 7906–7914.
51 A. L. D. Kilcoyne, T. Tyliszczak, W. F. Steele, S. Fakra, P. Hitchcock, K. Franck, E. Anderson, B. Harteneck, E. G. Rightor, G. E. Mitchell, A. P. Hitchcock, L. Yang, T. Warwick and H. Ade, *J. Synchrotron Radiat.*, 2003, **10**, 125–136.
52 R. J. Hopkins, K. Lewis, Y. Desyaterik, Z. Wang, A. V. Tivanski, W. P. Arnott, A. Laskin and M. K. Gilles, *Geophys. Res. Lett.*, 2007, **34**, L18806.
53 R. J. Hopkins, Y. Desyaterik, A. V. Tivanski, R. A. Zaveri, C. M. Berkowitz, T. Tyliszczak, M. K. Gilles and A. Laskin, *J. Geophys. Res.*, 2008, **113**, D04209.
54 H. A. Michelsen, A. V. Tivanski, M. K. Gilles, L. H. van Poppel, M. A. Dansson and P. R. Buseck, *Appl. Opt.*, 2007, **46**, 959–977.
55 A. V. Tivanski, R. J. Hopkins, T. Tyliszczak and M. K. Gilles, *J. Phys. Chem. A*, 2007, **111**, 5448–5458.
56 S. Takahama, S. Gilardoni, L. M. Russell and A. L. D. Kilcoyne, *Atmos. Environ.*, 2007, **41**, 9435–9451.
57 B. W. Arey, L. Kovarik, O. Qafoku, Z. Wang, N. J. Hess and A. R. Felmy, *Microsc. Microanal.*, 2013, **19**, 268–275.
58 M. Bailey and J. Hallett, *Q. J. R. Meteorol. Soc.*, 2002, **128**, 1461–1483.
59 M. Dymarska, B. J. Murray, L. Sun, M. L. Eastwood, D. A. Knopf and A. K. Bertram, *J. Geophys. Res.: Atmos.*, 2006, **111**, D04204.
60 M. L. Eastwood, S. Cremel, M. Wheeler, B. J. Murray, E. Girard and A. K. Bertram, *Geophys. Res. Lett.*, 2009, **36**, L02811.
61 R. Schaller and N. Fukuta, *J. Atmos. Sci.*, 1979, **36**, 1788–1802.
62 P. Roberts and J. Hallett, *Q. J. R. Meteorol. Soc.*, 1968, **94**, 25–34.
63 A. Welti, F. Luond, O. Stetzer and U. Lohmann, *Atmos. Chem. Phys.*, 2009, **9**, 6705–6715.
64 A. Salam, U. Lohmann, B. Crenna, G. Lesins, P. Klages, D. Rogers, R. Irani, A. MacGillivray and M. Coffin, *Aerosol Sci. Technol.*, 2006, **40**, 134–143.
65 T. Koop, B. P. Luo, A. Tsias and T. Peter, *Nature*, 2000, **406**, 611–614.
66 C. Marcolli, *Atmos. Chem. Phys.*, 2014, **14**, 2071–2104.
67 H. R. Pruppacher and J. D. Klett, *Microphysics of Clouds and Precipitation*, Kluwer Academic, Boston, USA, 2nd edn, 1997.
68 M. A. Freedman, *J. Phys. Chem. Lett.*, 2015, **6**, 3850–3858.
69 P. A. Alpert and D. A. Knopf, *Atmos. Chem. Phys.*, 2016, **16**, 2083–2107.
70 G. Ekosse, *Appl. Clay Sci.*, 2000, **16**, 301–320.
71 M. Zbik and R. S. Smart, *Clays Clay Miner.*, 1998, **46**, 153–160.
72 B. Bauluz, M. J. Mayayo, A. Yuste and J. M. González López, *Clay Miner.*, 2008, **43**, 459–475.
73 M. Valášková, M. Rieder, V. Matějka, P. Čapková and A. Slíva, *Appl. Clay Sci.*, 2007, **35**, 108–118.
74 G. J. Churchman, T. J. Davy, L. A. G. Aylmore, R. J. Gilkes and P. G. Self, *Clay Miner.*, 1995, **30**, 89–98.
75 I. D. Sills, L. A. G. Aylmore and J. P. Quirk, *J. Soil Sci.*, 1973, **24**, 480–490.
76 X. Woodward, A. Kostinski, S. China, C. Mazzoleni and W. Cantrell, *Aerosol Sci. Technol.*, 2015, **49**, 229–238.
77 T. Croteau, A. K. Bertram and G. N. Patey, *J. Phys. Chem. A*, 2009, **113**, 7826–7833.

78 S. J. Cox, Z. Raza, S. M. Kathmann, B. Slater and A. Michaelides, *Faraday Discuss.*, 2013, **167**, 389–403.
79 J. Um, G. M. McFarquhar, Y. P. Hong, S. S. Lee, C. H. Jung, R. P. Lawson and Q. Mo, *Atmos. Chem. Phys.*, 2015, **15**, 3933–3956.
80 M. Bailey and J. Hallett, *J. Atmos. Sci.*, 2012, **69**, 390–402.
81 M. P. Bailey and J. Hallett, *J. Atmos. Sci.*, 2009, **66**, 2888–2899.
82 T. Koop, J. Bookhold, M. Shiraiwa and U. Pöschl, *Phys. Chem. Chem. Phys.*, 2011, **13**, 19238–19255.
83 S. T. Martin, *Chem. Rev.*, 2000, **100**, 3403–3453.
84 M. Yeşilbaş and J. F. Boily, *J. Phys. Chem. Lett.*, 2016, **7**, 2849–2855.